Spectrochimica Acta Part A: Molecular and Biomolecular Spectroscopy 343 (2025) 126495

Contents lists available at ScienceDirect

Spectrochimica Acta Part A:
Molecular and Biomolecular Spectroscopy

journal homepage: www.journals.elsevier.com/spectrochimica-acta-part-a-molecular-and-biomolecular-spectroscopy

Tailoring Nonlinear Optical Response: Impact of Substituents in Thiazole-Azo Polymers

Karolina Waszkowska [a,*], Vitaliy Smokal [b,*], Mustafa Karakaya [c], Asli Karakas [d,*], Andriy V. Kityk [e], Anna Migalska-Zalas [f], Bouchta Sahraoui [a]

[a] Univ Angers, LPhiA, SFR MATRIX, F-49000 Angers, France
[b] Taras Shevchenko National University of Kyiv, 64/13 Volodymyrska St., 01601 Kyiv, Ukraine
[c] Sinop University, Faculty of Engineering & Architecture, Department of Energy Systems, Sinop, Turkey
[d] Selcuk University, Faculty of Sciences, Department of Physics, Campus, Konya, Turkey
[e] Faculty of Electrical Engineering, Częstochowa University of Technology, Al. Armii Krajowej 17, 42-200 Częstochowa, Poland
[f] Faculty of Science and Technology, Jan Dlugosz University in Czestochowa, Al. Armii Krajowej 13/15, 42-201 Czestochowa, Poland

HIGHLIGHTS

- Impact of substituents on NLO properties of thiazole-azo polymer films.
- Remarkable NLO response in 2-methyl-5-benzothiazolyl moiety, enhanced charge transfer.
- Enhanced SHG performance of thiazole-azo polymers compared to styrylquinoline polymers.
- Optimized thiazole-azo polymers for NLO applications.
- Good agreement with DFT calculations on second- and third-order susceptibilities.

GRAPHICAL ABSTRACT

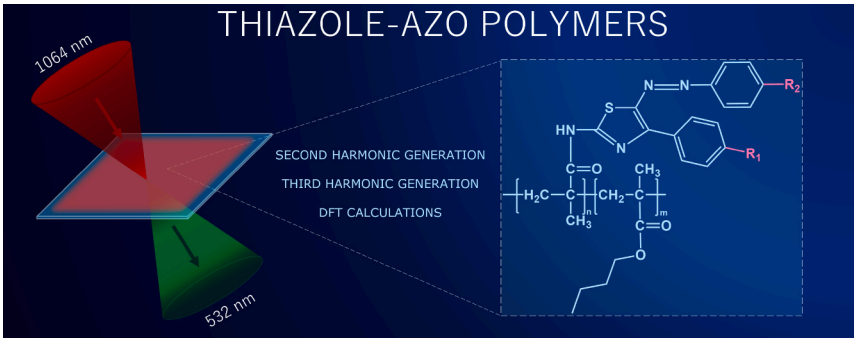

ARTICLE INFO

Keywords:
DFT
Hyperpolarizability
MO analyze
Nonlinear optics
Nonlinear susceptibility
Second Harmonic generation
Thiazole-Azo polymers
Third Harmonic generation

ABSTRACT

This study explores how different chemical substituents impact the nonlinear optical (NLO) behavior of specialized thiazole-azo polymer thin films. Using the well-known Maker fringe technique, we dive into their second- and third-harmonic generation capabilities (SHG and THG, respectively), revealing key NLO parameters such as second- and third-order susceptibility. The findings show that these thiazole-azo polymers exhibit impressive NLO responses, positioning them as strong candidates for advanced optoelectronic applications driven by NLO phenomena. These materials, with their remarkable NLO enhancements, hold promise for the future optical devices. To investigate the microscopic second- and third-order NLO phenomena of title structures, we compute the electric dipole moments (μ), static and dynamic dipole polarizabilities (α), second-order (β) and third-order (γ) hyperpolarizabilities using density functional theory (DFT). We calculate the frequency-dependent second- ($\chi^{(2)}$) and third-order ($\chi^{(3)}$) susceptibilities through the time-dependent Hartree-Fock (TDHF) technique. The one-photon absorption (OPA) properties of the examined thin films are also computed, and both theoretical and experimental UV–Vis spectra are presented. Furthermore, the outcomes of the analyzed

* Corresponding authors.
E-mail addresses: karolina.waszkowska@univ-angers.fr (K. Waszkowska), vitalii.smokal@knu.ua (V. Smokal), akarakas@selcuk.edu.tr (A. Karakas).

https://doi.org/10.1016/j.saa.2025.126495
Received 5 March 2025; Received in revised form 19 May 2025; Accepted 29 May 2025
Available online 31 May 2025

and simulated OPA spectra, ($\chi^{(2)}$) and ($\chi^{(3)}$) susceptibilities are compared to highlight their compatibility. The investigated materials demonstrate significant quadratic and cubic hyperpolarizabilities and susceptibilities with non-zero values, showcasing substantial second- and third-order optical nonlinearity. To enhance understanding of the molecular orbital (MO) structures, we interpret the highest occupied molecular orbitals (HOMOs), lowest unoccupied molecular orbitals (LUMOs), and HOMO–LUMO energy gaps from DFT.

1. Introduction

Nonlinear optical (NLO) properties are critical in the development of advanced photonic and optoelectronic technologies, including optical switching, frequency doubling, and signal processing applications [1–3]. Among the NLO processes, second harmonic generation (SHG) and third harmonic generation (THG) are of the particular interest due to their applicability in photonic devices [4]. SHG is widely used with applications spanning both fundamental research and practical technologies [5]. It plays a key role in frequency doubling of laser light, such as converting 1064 nm infrared output into visible green light at 532 nm [6]. Additionally, SHG imaging is extensively employed in biomedical fields for high-resolution, label-free visualization of non-centrosymmetric biological structures like collagen, aiding in cancer diagnostics and tissue pathology analysis [7–9]. Moreover, SHG is a powerful tool for characterizing material symmetry, enabling rapid detection of noncentrosymmetry in both crystalline and powdered samples [10,11]. Furthermore, THG effects play a vital role in a range of modern photonic applications [12]. These include phase conjugation through wave mixing techniques, ultrafast laser pulse generation via mode-locking, and NLO absorption phenomena such as two-photon absorption (TPA) and reverse saturable absorption (RSA) [13–15]. TPA enables high-resolution 3D optical data storage and biomedical imaging [16,17], while RSA is used in optical limiting to protect sensitive components from high-intensity laser exposure [18]. Third order nonlinearities are also fundamental to Q-switching, a technique for generating high-energy laser pulses, as well as optical bistability, used in optical switching and memory elements [19,20]. Other key THG effects include the photorefractive effect, used in dynamic holography, and self-phase modulation, which enables spectral broadening of pulses in optical fibres [21–23]. Numerous materials exhibit NLO behaviour, and the search for novel compounds with enhanced NLO responses still continues.

Within the scope of NLO materials, polymers containing chromophores, such as azobenzene derivatives, have garnered significant interest due to their highly tuneable optical properties [24–32]. The structural flexibility in azobenzene-containing polymers enables adjustments in their electronic and dipole configurations, making them ideal candidates for effective second (SHG) and third harmonic generation (THG) responses, essential for NLO device applications [33–35]. The advantage of azobenzene polymers in the field of NLO lies in their tuneable electronic structure, influenced by electron-donating or electron-withdrawing substituents [35,36]. These substituents can induce hypsochromic or bathochromic shifts, thus affecting the materials' electronic transitions and the efficiency of NLO processes [37,38]. Such modifications are crucial in optimizing azobenzene polymers to achieve desired NLO behaviours for specific applications. Azopolymers also demonstrate notable compatibility with various polymer matrices and copolymer units, allowing for the synthesis of hybrid materials with tailored NLO responses [39,40]. This adaptability is beneficial in creating materials that combine azobenzene's NLO activity with the mechanical or thermal stability of the polymer matrix, enhancing the practical applications of these materials in areas like optical modulators, holography, and data storage technologies [41–44]. In the recent years, an increased attention has been devoted to thiazole-azo materials due to the electron-withdrawing nature of the thiazole ring and its conjugated characteristics [45]. This structural framework, which promotes an enhanced intramolecular charge transfer (ICT), is particularly advantageous for NLO applications [46,47]. Notably, recent literature has underlined the potential of thiazole-azo materials for the integration into the photonic devices [48–50], however a systematic theoretical and experimental analysis on the NLO properties still remain limited.

The present study aims to introduce experimentally and theoretically fundamental principles of NLO responses in thiazole-azo polymers, focusing particularly on their SHG and THG characteristics. The selected polymers (**P1**-**P4**) feature systematically varied substituents, ranging from electron-withdrawing to electron-donating groups, to investigate the structural property relationship and its influence on the NLO behaviour of thiazole-azo systems. Firstly, utilizing the Maker fringe technique, the research evaluates their NLO responses, comparing variations in their second- and third-order susceptibilities across different chemical structures. Given the increasing interest in thiazole-azo based polymers for high-performance NLO applications, this study seeks to clarify how molecular modifications impact their NLO behaviour, positioning them as promising candidates for optoelectronic technologies. Secondly, the electric dipole moments, dispersion-free and frequency-dependent dipole polarizabilities, second- and third-order hyperpolarizability values and susceptibilities for the examined materials have been explored from DFT (μ, static and dynamic α, β, γ) and ab initio (dynamic $\chi^{(2)}$ and $\chi^{(3)}$) processes. Besides the optical nonlinearity characteristics, the frontier MO energies (first and second) and OPA wavelengths exposed to the lowest lying electronic transitions for title materials have been presented by the DFT/ B3LYP and TD-SCF/ HF techniques, respectively. The computed data on OPA wavelengths (λ_{max}) (i.e. UV–Vis wavelengths), $\chi^{(2)}$ and $\chi^{(3)}$ susceptibility have been compared with the experimental conclusions introduced via the UV–Vis spectral analyses, and the SHG and THG experiments. Our calculated yields in this work have been also tried to match some data already published for similar structures and with the consequences of reference items utilized in NLO measurements.

2. Experimental methods

2.1. Optical absorption

UV–Vis absorption spectra were recorded with a UV-1800 spectrometer (Shimadzu) at room temperature within the range of 300 nm to 1100 nm.

2.2. Maker fringe

SHG and THG effects were investigated using a Maker fringe setup [51–53]. An ultrafast Nd:YAG laser, operating at a wavelength 1064 nm with beam diameter 40 μm, pulse duration of 30 ps, repetition rate of 10 Hz, resulting in a peak intensity of 239 GW/cm^2, was used as the pump source. SHG and THG Maker fringes were obtained by rotating thin films on a rotational stage under two laser polarization configurations: *sp* (perpendicular to the plane of incidence) and *pp* (parallel to the plane of incidence), controlled by a Glan polarizer. During rotation, the sample generated signal corresponding to ω, 2ω, 3ω, and higher-order harmonics, which were then detected by a photomultiplier tube. Before the signal reached the photomultiplier tube, the desired signal was filtered through an interference filter: a 532 nm was used for SHG measurements, and a 355 nm filter was used for THG measurements.

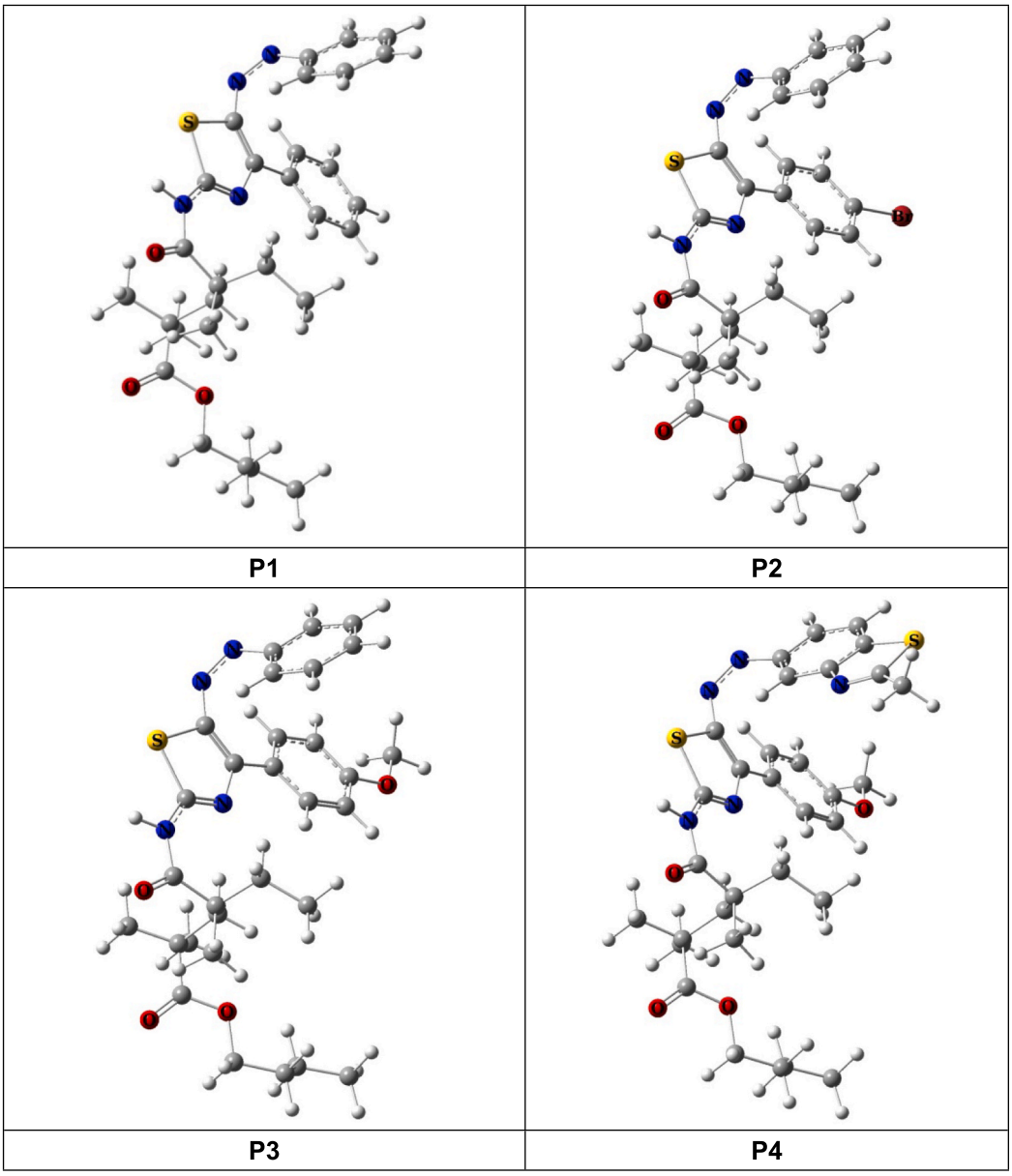

Fig. 1. Optimized molecular models of the thiazole-azo copolymers **P1**-**P4**. C, N, H, O, S and Br atoms correspond to grey, blue, white, red, yellow and claret red ball-shaped, respectively.

2.3. Corona poling

Methods such as the corona poling technique are widely used to break the centrosymmetry in polymeric films by aligning polar chromophores under an external electric field [54,55]. In this home-made approach, thin films were heated to a temperature close to the glass transition temperature (below 100 °C), and a high voltage of 6 kV was applied. This process enables us to reorient the dipole moments in the heated material of polymer molecules, aligning them with the direction of the applied electric field. Once the corona poling system was deactivated, the oriented dipole moments remained aligned.

3. Computational studies

Primarily, the tasks of geometry optimization have been exerted on the title thiazole-azo polymers (see Fig. 1). Then, the electric dipole moment, static and dynamic dipole polarizability, quadratic and cubic hyperpolarizability qualifications have been gotten operating calculation procedures. The finite field (FF) method has been taken advantage of calculating μ, α, β and γ [56]. The FF technique submits a worthy venture to the hyperpolarizability tensors [57]. The geometry optimization labors with 3–21G basis set, computations of μ, α, β and γ with both 6–31 + G(d) diffused and polarized basis set and also 3–21 + G diffused basis set for title molecules have been produced from GAUSSIAN09W [58] program operating DFT/ B3LYP (geometry optimizations and μ, α, β, γ values) and DFT/ PBE (μ, α, β, γ values). To contrive the configurations of molecular structures for the title materials, we have operated the GaussView 5.0.9 [59] program for the interface software of GAUSSIAN09W [58]. The efficiencies of DFT approximations have been openly sighted in the literature [60]. For extracting the hyperpolarizability tensorial components of molecular organic constitutions, the B3LYP functional is one of the most opportune ways [61,62]. This functional is generally submitted to compose admissible experimental arrangements [63]. To reveal the influence of functional choices on μ, α, β, γ results, the PBE that is gradient-corrected correlation functional of Perdew, Burke and Ernzerhof [64] has been

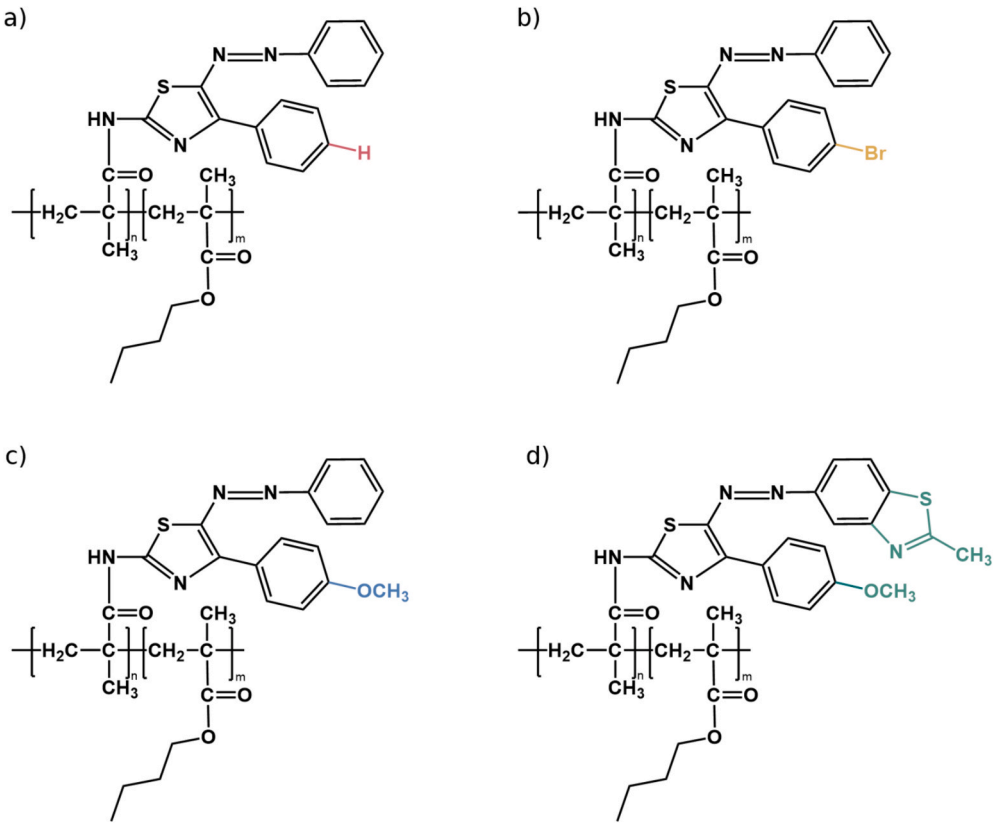

Fig. 2. Chemical structures of studied thiazole-azo copolymers **P1** (a), **P2** (b), **P3** (c) and **P4** (d).

also utilized in our DFT calculations. The equations (1–3), respectively, have been exploited for computing the orientationally averaged (isotropic) dipole polarizabilities ⟨α⟩, total first hyperpolarizabilities β_{tot} and averaged (isotropic) second hyperpolarizability ⟨γ⟩ [65]:

$$\langle\alpha\rangle - \left(\alpha_{xx} + \alpha_{yy} + \alpha_{zz}\right)/3 \tag{1}$$

$$\beta_{tot} = \left[\left(\beta_{xxx} + \beta_{xyy} + \beta_{xzz}\right)^2 + \left(\beta_{yyy} + \beta_{yzz} + \beta_{yxx}\right)^2 + \left(\beta_{zzz} + \beta_{zxx} + \beta_{zyy}\right)^2\right]^{1/2} \tag{2}$$

$$\langle\gamma\rangle = (1/5)\left[\gamma_{xxxx} + \gamma_{yyyy} + \gamma_{zzzz} + 2\left(\gamma_{xxyy} + \gamma_{xxzz} + \gamma_{yyzz}\right)\right] \tag{3}$$

The GAUSSIAN09W [58] program propagated the α(0;0), β(0;0,0) and γ(0;0,0,0) at ω = 0 and α(–ω;ω), β(–2ω;ω,ω), γ(–3ω;ω,ω,ω) values of tensor components at ω = 0.04282 atomic units (a.u.) (1064 nm) via the DFT technique with basis sets 6–31 + G(d) and 3–21 + G. The dispersion-free quadratic and cubic hyperpolarizability constituents designated above are characterized as β(0;0,0) and γ(0;0,0,0), respectively. The SHG and THG groups in the DFT technique have been employed to compute the β (–2ω;ω,ω) and γ(–3ω;ω,ω,ω), respectively, at ω values of laser frequency operated in the NLO measurements.

We have discovered the isotropic (orientationally averaged) values for the second- $\langle\chi^{(2)}(-\omega;\omega,0)\rangle$ and third-order $\langle\chi^{(3)}(-\omega;\omega,-\omega,\omega)\rangle$ susceptibilities at ω = 0.04282 a.u. from electro-optics Pockels effect (EOPE) group and optical Kerr effect (OKE) group, respectively, of the TDHF method with 6–31 + G(d) and 3–21 + G basis sets enforced in the GAMESS [66] program. The origins of Cartesian coordinate systems (*x*,*y*, *z*) = (0,0,0) in all calculations here have been selected on the centres of masses of **P1**-**P4**.

The TD-SCF/ HF approximation with cc-pVDZ basis set implemented in the GAUSSIAN09W [58] program has accomplished the calculations of transition wavelengths (λ_{max}) for the lowest lying electronic transitions of **P1**-**P4**. To acknowledge the contact of NLO qualities with the molecular forms; the first and second frontier MOs and their energy gaps have also been accomplished from GAUSSIAN09W [58] program at DFT/ B3LYP/ 6-31+G(d) level of theory. The HOMO–LUMO energy gap (E_g) could be designated by the equation (4):

$$E_g = E_{LUMO} - E_{HOMO} \tag{4}$$

The correlation between the wavelengths of light emitted or absorbed (λ) from an item and HOMO-LUMO energy gaps (E_g) is characterized as follows:

$$E_g = \frac{h \bullet c}{\lambda} \tag{5}$$

where *h* is Planck' s constant and *c* is the speed of light.

4. Results and discussion

4.1. Samples preparation

The synthesis of thiazole-azo monomers has been previously reported [67,68]. The copolymers, namely: **P1**; **P2**; **P3**; and **P4** have been synthesized by the method of free radical polymerization azo containing methacrylic monomers and butyl methacrylate (BMA) in 10 % dimethylformamide (DMF) solution with azobisisobutyronitrile (AIBN) as radical initiator at 80 °C (argon atmosphere) with monomers initial mole ratios 1:1 and AIBN (1 wt% of monomer). The synthesis procedure for the polymer is described in the Supporting Information (ESI). The characteristic ^{1}H NMR signals of the thiazole-azo monomers have been previously reported [67,68]. In this study, NMR was used to determine the molar ratio of the azo monomer to BMA in copolymers **P1**-**P4** by comparing the integrals of aromatic (δ 6.5–8.5 ppm) and aliphatic proton regions (Figs. S1-S4). Fourier-transform infrared (FTIR) spectroscopy was used to confirm the chemical structure of the synthesized polymers. The corresponding spectra and analysis are presented in the

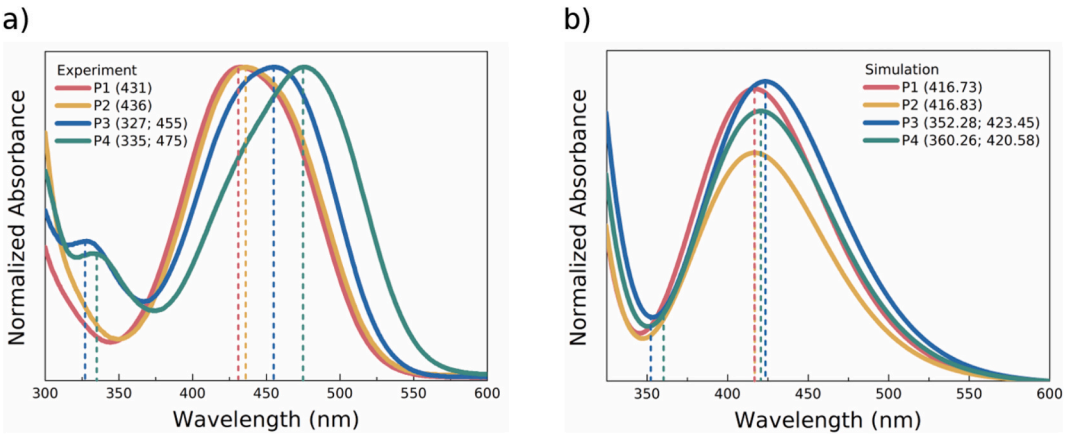

Fig. 3. Experimental UV–Vis absorption spectra (a) for **P1**-**P4** together with their corresponding theoretical data (b). The solid and dashed lines display the main measurement and simulation absorption peaks obtained from the UV–Vis recording spectrophotometer and TD-SCF/ HF computations with cc-pVDZ basis set, respectively.

Table 1
Maximum absorption peaks (λ_{max}), values of absorption coefficients at THG (α_{355}) and SHG (α_{532}) wavelengths of studied **P1**-**P4** thiazole-azo polymeric thin films.

Sample	λ_{max} (nm)	α_{355} (cm^{-1})	α_{532} (cm^{-1})
P1	431	2248	882
P2	436	2043	981
P3	327; 455	4372	1563
P4	335; 475	4859	5357

ESI (Figs. S5-S8). The differential scanning calorimetry (DSC) analysis results, demonstrate that the thiazole-azo copolymers **P1**-**P4** exhibit glass transition temperatures (T_g) in the range of 90 to 98 °C. The size exclusion chromatography (SEC) was utilized to measure the number-average molecular weight (M_n) and dispersity (Đ) for polymers **P1**-**P4**, with polystyrene as the calibration standard. The dispersity values for these synthesized polymers ranged from 1.7 to 1.9, indicating a reasonable degree of polydispersity for the methacrylic polymers. The molecular weights of the copolymers **P1**-**P4** molecular rations, index of polydispersity, glass transition temperatures (T_g) are summarized in Table S1. The chemical structures of **P1**-**P4** are displayed in Fig. 2. Thiazole-azo polymeric thin films were deposited on BK7 glass substrate using spin coating technique with 1000 rpm for 60 s from 10 wt% 1,2-dichloroethane solution. Thickness of the thin films was determined using profilometer (Dektak 6 M), and is equal to 1.30 μm for **P1**, 0.90 μm for **P2**, 1.00 μm for **P3**, and 0.83 μm for **P4**. While auxiliary techniques such as ellipsometry were not employed to cross-validate the thickness measurements in this study, previous research on the same polymer samples (though with different thin films) confirmed their homogeneity and smoothness [68]. Thickness values of 353 ± 1 nm, 479 ± 1 nm, 645 ± 1 nm, and 555 ± 1 nm for these samples were determined using spectroscopic ellipsometry, and surface roughness measurements from AFM (R_a: 0.15–0.36 nm) confirmed the smoothness of these films, supporting the reliability of the profilometer-derived thickness data for the samples in this work [68].

4.2. Optical absorption spectroscopy

Fig. 3(a) presents the normalized absorption spectra recorded experimentally via UV–Vis spectrophotometer of thiazole-azo polymeric thin films, highlighting absorption bands within the range of 350 – 600 nm. Noticeable peaks in Fig. 3(a) appear at 431 nm for **P1**, 436 nm for **P2**, 455 nm for **P3**, and 475 nm for **P4**, attributed to vibrational coupling during the n → π* transition. Notably, **P3** and **P4** feature an additional peak between 300 – 350 nm, with a maximum at 327 nm for **P3** and 335 nm for **P4**, linked to electron-donor substituents in the aromatic 4-aryl-1,3-thiazol-2-amine ring. The observed red shift in the absorption wavelength for copolymer **P4** is attributed to the extension of the conjugation length within the polymer. Beyond 600 nm, thin films exhibit excellent optical transparency, showing no absorption up to 1100 nm, making them ideal for applications at the fundamental laser wavelength of 1064 nm (see Fig. 3(a)). However, the films absorb strongly at second (532 nm) and third (355 nm) harmonic wavelengths, potentially influencing harmonic generation. Absorption coefficients (α) at these key wavelengths experimentally obtained (see Fig. 3(a)) are provided in Table 1, illustrating the influence of material design on harmonic generation efficiency. For comparison, the theoretical absorption spectra obtained via TD-SCF/HF calculations with the cc-pVDZ basis set are shown in Fig. 3(b) and are discussed in detail in Section 4.5.

4.3. Second and third harmonic generations

NLO research was conducted based on SHG and THG effects. The NLO signal, separated by an appropriate filter positioned just behind the sample, was collected using a photomultiplier. To ensure measurement accuracy and material integrity, experiments were performed at a laser energy of 100 μJ, which is below damage thresholds reported in similar studies (e.g., 150 μJ) [69], ensuring operation within the linear regime. Moreover, while harmonic signal intensity increases with sample thickness due to greater optical interaction path, the extracted NLO susceptibility values remain independent of thickness, as they are intrinsic material properties [70]. To reduce variability, samples with comparable and uniform thickness were selected. Initially, the SHG and THG signals of reference materials: Y-cut quartz slab and fused silica, respectively, were measured (see Figs. S9-S10). Following this, the SHG properties of thiazole-azo polymeric thin films were investigated. The initial absence of SHG signal confirms that the polymer films are initially centrosymmetric, as SHG is forbidden in such media under the electric-dipole approximation. Upon application of the corona poling method, a clear SHG response emerges (see Fig. 4), confirming the successful alignment of molecular dipoles and the induction of non-centrosymmetric order necessary for second-order NLO processes. Notably, under *pp* polarization the SHG signal exhibited a significant enhancement compared to *sp* polarization. This difference is due to the varying values of the $\chi^{(2)}$ tensor elements relevant to each experimental setup, specifically, $\chi^{(2)}_{zzz}$ and $\chi^{(2)}_{zxx}$. Theoretically, the ratio $\chi^{(2)}_{zzz}/\ \chi^{(2)}_{zxx}$ is predicted to be approximately 3 for molecular systems [71].The graphical analysis of the SHG responses indicates that the SHG intensities remain consistent across the samples with various substituents,

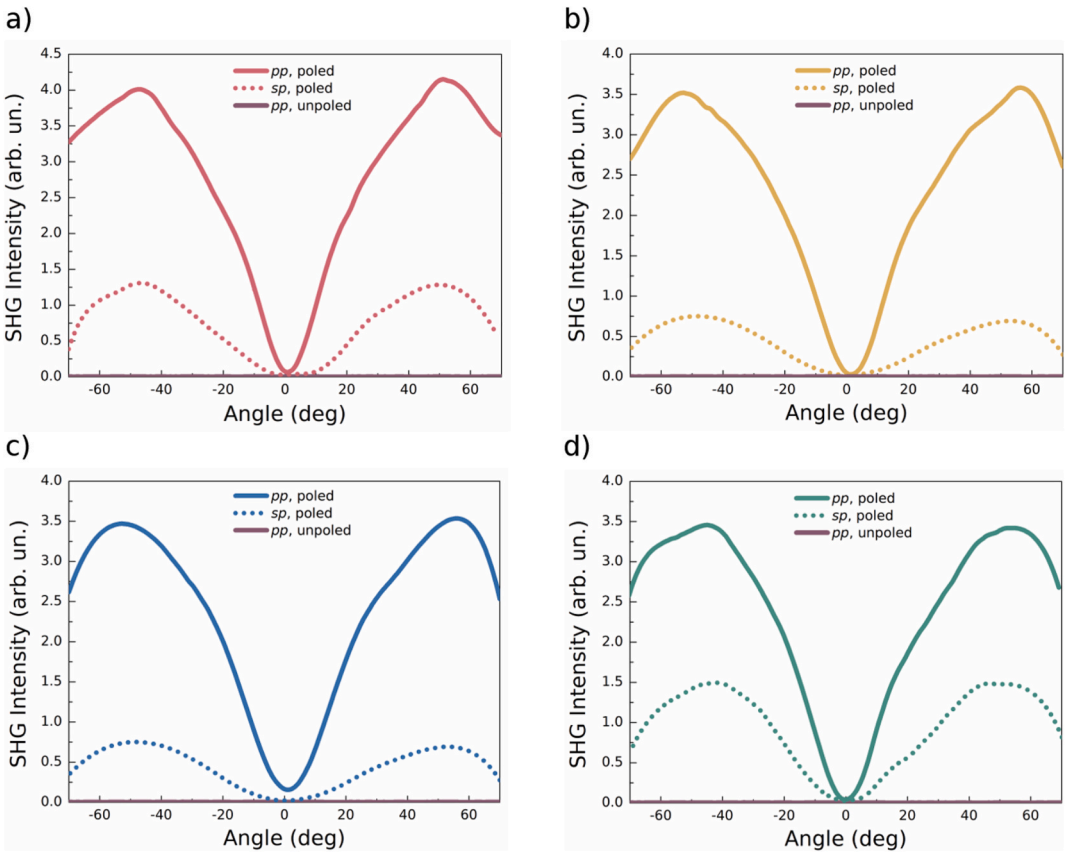

Fig. 4. SHG response as a function of incident angle of thiazole-azo thin **P1** (a), **P2** (b), **P3** (c) and **P4** (d) films before (unpoled) and after (poled) corona poling technique in *sp* and *pp* polarization configurations at 1064 nm.

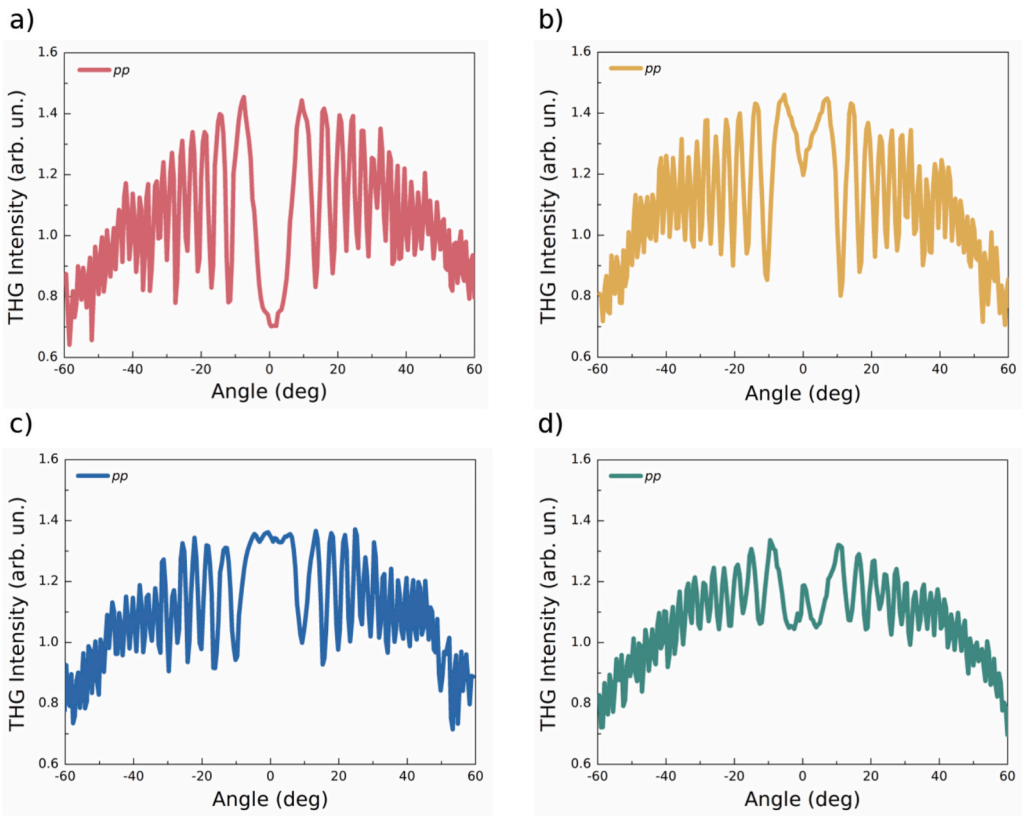

Fig. 5. THG response as a function of incident angle of studied thiazole-azo thin films **P1** (a), **P2** (b), **P3** (c) and **P4** (d) in *pp* polarization configuration at 1064 nm.

Table 2
Second- ($\chi^{(2)}$) and third-order ($\chi^{(3)}$) NLO susceptibilities obtained by experimental studies for *sp* and *pp* polarization configurations with ~ 0.1 % estimated error and averaged (isotropic) second- ($\langle\chi^{(2)}(-\omega;\omega,0)\rangle$) and third-order ($\langle\chi^{(3)}(-\omega;\omega,-\omega,\omega)\rangle$) NLO susceptibilities calculated by TDHF procedure using 6–31 + G(d) and 3–21 + G basis sets at 1064 nm of **P1**-**P4**.

Sample	$\chi^{(2)}$ (pm.V^{-1})		$\langle\chi^{(2)}\rangle$ (pm.V^{-1})		$\chi^{(3)} \times 10^{-22}$ (m^2.V^{-2})		$\langle\chi^{(3)}\rangle \times 10^{-22}$ (m^2.V^{-2})	
	sp	*pp*	6–31 + G(d)	3–21 + G	*sp*	*pp*	6–31 + G(d)	3–21 + G
P1	0.28	0.60	0.85	0.11	7.04	7.16	9.01	3.81
P2	0.31	0.89	1.03	0.19	9.81	10.05	12.77	5.88
P3	0.35	0.70	0.96	0.15	9.25	9.55	11.90	5.10
P4	0.49	1.03	2.11	0.20	10.64	11.05	13.00	6.20

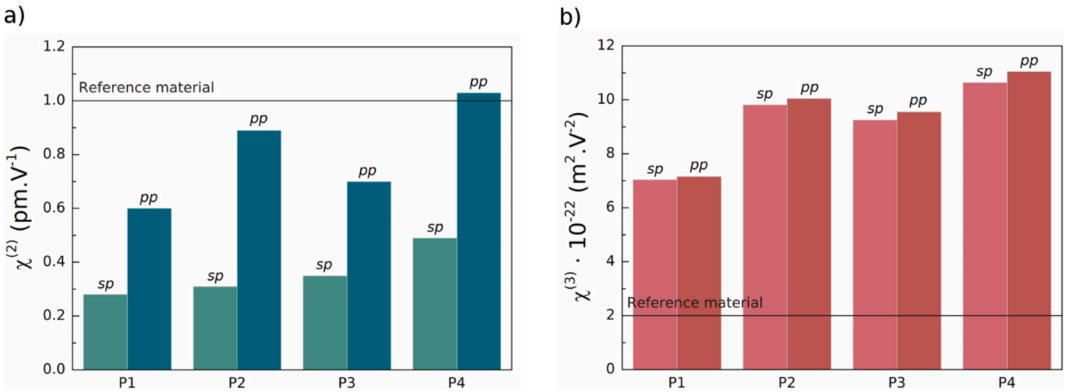

Fig. 6. Graphical representation of the second-order (left) and third-order (right) NLO susceptibility values of **P1**-**P4** thiazole-azo thin films for *sp* and *pp* polarization configurations at 1064 nm.

Table 3
The calculated electric dipole moments μ (Debye) and dipole moment components using DFT at B3LYP/ 6–31 + G(d), B3LYP/ 3–21 + G, PBE/ 6–31 + G(d), PBE/ 3–21 + G levels of theory for **P1**-**P4**.

Compound	Functional/ Basis set	μ_x	μ_y	μ_z	μ
P1	B3LYP/ 6–31 + G(d)	0.000	0.000	6.986	6.986
	B3LYP/ 3–21 + G	0.000	0.000	6.328	6.328
	PBE/ 6–31 + G(d)	0.000	0.000	3.163	3.163
	PBE/ 3–21 + G	0.000	0.000	3.495	3.495
P2	B3LYP/ 6–31 + G(d)	0.000	0.000	5.439	5.439
	B3LYP/ 3–21 + G	0.000	0.000	5.087	5.087
	PBE/ 6–31 + G(d)	0.000	0.000	3.192	3.192
	PBE/ 3–21 + G	0.000	0.000	3.111	3.111
P3	B3LYP/ 6–31 + G(d)	0.000	0.000	7.176	7.176
	B3LYP/ 3–21 + G	0.000	0.000	6.635	6.635
	PBE/ 6–31 + G(d)	0.000	0.000	3.209	3.209
	PBE/ 3–21 + G	0.000	0.000	3.516	3.516
P4	B3LYP/ 6–31 + G(d)	0.000	0.000	7.451	7.451
	B3LYP/ 3–21 + G	0.000	0.000	6.819	6.819
	PBE/ 6–31 + G(d)	0.000	0.000	5.137	5.137
	PBE/ 3–21 + G	0.000	0.000	4.754	4.754

Table 4
Selected components of the static α(0;0) and ⟨α⟩(0;0) ($\times 10^{-24}$ esu) values computed by DFT at B3LYP/ 6–31 + G(d), B3LYP/ 3–21 + G, PBE/ 6–31 + G(d), PBE/ 3–21 + G levels of theory for **P1**-**P4**.

Compound	Functional/ Basis set	α_{xx}	α_{yy}	α_{zz}	⟨α⟩
P1	B3LYP/ 6–31 + G(d)	53.828	43.569	50.888	49.428
	B3LYP/ 3–21 + G	51.546	41.762	48.245	47.185
	PBE/ 6–31 + G(d)	33.843	30.991	28.900	31.245
	PBE/ 3–21 + G	33.851	29.527	28.851	30.743
P2	B3LYP/ 6–31 + G(d)	54.725	51.191	49.565	51.827
	B3LYP/ 3–21 + G	52.649	49.126	46.782	49.519
	PBE/ 6–31 + G(d)	38.090	38.639	26.391	34.374
	PBE/ 3–21 + G	36.355	36.346	24.077	32.259
P3	B3LYP/ 6–31 + G(d)	52.553	44.700	58.292	51.848
	B3LYP/ 3–21 + G	50.365	42.408	55.847	49.540
	PBE/ 6–31 + G(d)	32.285	30.785	36.104	33.058
	PBE/ 3–21 + G	32.890	28.878	35.872	32.547
P4	B3LYP/ 6–31 + G(d)	56.256	56.571	62.845	58.558
	B3LYP/ 3–21 + G	53.710	54.232	59.953	55.965
	PBE/ 6–31 + G(d)	35.437	38.519	39.259	37.738
	PBE/ 3–21 + G	34.572	37.173	38.249	36.665

including –H (**P1**), –Br (**P2**), and –OCH_3 (**P3**). This uniformity in SHG signal intensity suggests that while the electronic properties of the substituents vary, they do not significantly influence the overall SHG efficiency within this polymer structure. The similarity in SHG response across different substituents could be attributed to the inherent symmetry or electronic structure of the thiazole-azo polymer backbone, which may play a dominant role in defining the NLO susceptibility. Even though substituents like –Br, with higher polarizability, and –OCH_3, an electron-donating group, might be expected to alter the electron distribution and thus the SHG signal, the consistent SHG intensities suggest that the core electronic configuration and dipole alignment in the polymer are maintained across modifications.

In the second stage, the measurement was repeated with a setting the inference filter to 355 nm, allowing collection of the THG signal. The results of the THG measurements conducted are presented in Fig. 5. Generally, no significant changes in polarization measurements were observed for these samples. Like the SHG studies, the relationships in the third-order NLO response exhibited diversity with respect to substituents. On the other hand, THG trends show some variation among samples, with a slight increase in THG response for the sample containing the –H (**P1**) and –Br (**P2**) compared to the 2-methyl-5-benzothiazolyl and –OCH_3 substituent (**P4** and **P3**) counterparts. It is essential to

Table 5
Selected components of the static β(0;0,0) and β_{tot}(0;0,0) ($\times 10^{-33}$ esu) values computed by DFT at B3LYP/ 6–31 + G(d), B3LYP/ 3–21 + G, PBE/ 6–31 + G(d), PBE/ 3–21 + G levels of theory for **P1**-**P4**.

Compound	Functional/ Basis set	β_{xxx}	β_{yyy}	β_{yyz}	β_{xzz}	β_{zzz}	β_{tot}
P1	B3LYP/ 6–31 + G(d)	831.775	269.140	−521.165	−170.757	−453.111	1936.553
	B3LYP/ 3–21 + G	712.586	99.828	−274.936	−87.710	−291.194	1702.443
	PBE/ 6–31 + G(d)	193.694	131.871	290.685	−184.530	−731.824	894.355
	PBE/ 3–21 + G	303.408	262.071	353.076	−118.776	−510.207	1172.996
P2	B3LYP/ 6–31 + G(d)	418.335	−1431.430	−880.678	15.112	−1923.350	2167.263
	B3LYP/ 3–21 + G	246.987	−1567.330	−783.302	89.553	−1497.160	2402.884
	PBE/ 6–31 + G(d)	−605.507	1151.050	−569.022	194.642	−803.747	2649.821
	PBE/ 3–21 + G	−276.483	−1166.760	263.442	260.875	−810.026	642.803
P3	B3LYP/ 6–31 + G(d)	735.979	−382.976	−2154.460	−1590.310	−994.967	2873.358
	B3LYP/ 3–21 + G	730.672	−687.616	−2010.560	−1474.980	−804.437	2537.273
	PBE/ 6–31 + G(d)	299.337	−2332.850	−1115.090	−1036.940	115.651	2719.425
	PBE/ 3–21 + G	379.500	−1747.810	−1128.700	−1002.510	−16.773	2165.645
P4	B3LYP/ 6–31 + G(d)	879.381	1292.050	−2789.250	−1262.98	−1212.250	4253.807
	B3LYP/ 3–21 + G	942.072	817.689	−2606.300	−1165.650	−1170.930	3722.352
	PBE/ 6–31 + G(d)	403.184	−1447.980	−1134.450	−952.553	−1151.740	3085.297
	PBE/ 3–21 + G	612.529	−932.566	−1317.230	−818.707	−1133.630	2766.502

Table 6
Selected components of the static γ(0;0,0,0) and ⟨γ⟩(0;0,0,0) ($\times 10^{-37}$ esu) values computed by DFT at B3LYP/ 6–31 + G(d), B3LYP/ 3–21 + G, PBE/ 6–31 + G(d), PBE/ 3–21 + G levels of theory for **P1**-**P4**.

Compound	Functional/ Basis set	γ_{xxxx}	γ_{yyyy}	γ_{zzzz}	γ_{xxyy}	γ_{xxzz}	γ_{yyzz}	⟨γ⟩
P1	B3LYP/ 6–31 + G(d)	245.128	98.495	126.528	37.724	76.332	86.936	174.427
	B3LYP/ 3–21 + G	217.779	93.082	111.701	34.173	69.785	77.160	156.960
	PBE/ 6–31 + G(d)	117.592	119.783	86.713	18.480	34.131	17.914	93.028
	PBE/ 3–21 + G	131.524	91.469	70.216	22.903	31.658	25.371	90.615
P2	B3LYP/ 6–31 + G(d)	265.461	193.395	165.745	4.756	56.938	82.332	182.531
	B3LYP/ 3–21 + G	239.384	289.683	146.379	1.387	52.956	72.797	185.945
	PBE/ 6–31 + G(d)	181.769	233.629	75.861	5.104	14.738	64.544	132.006
	PBE/ 3–21 + G	180.216	222.166	78.716	0.116	19.222	12.270	108.863
P3	B3LYP/ 6–31 + G(d)	192.120	150.762	202.684	23.928	108.907	133.796	215.766
	B3LYP/ 3–21 + G	168.683	142.297	183.278	21.168	98.446	127.047	197.516
	PBE/ 6–31 + G(d)	62.039	175.186	131.867	6.324	63.129	57.420	124.568
	PBE/ 3–21 + G	89.240	132.044	107.005	9.086	60.370	67.851	120.581
P4	B3LYP/ 6–31 + G(d)	157.605	254.351	220.415	63.301	123.004	161.493	265.593
	B3LYP/ 3–21 + G	138.706	228.822	200.023	61.166	112.539	151.570	243.620
	PBE/ 6–31 + G(d)	47.978	186.275	187.751	45.217	52.587	67.606	150.565
	PBE/ 3–21 + G	58.991	160.043	151.428	43.746	53.797	73.390	142.466

calculate the values of $\chi^{(2)}$ and $\chi^{(3)}$ to determine which copolymers exhibits the highest NLO response, which is provided in the next subchapter.

4.4. NLO susceptibility

Second- and third-order NLO susceptibilities were determined from SHG and THG experiments, respectively, through the comparative models. These models are based on comparison the generated harmonics' maximum intensity of studied material to that of the reference material. In our case, we used 0.5 mm Y-cut quartz slab for SHG experiment, and 1 mm fused silica for THG experiment. Moreover, as previously mentioned, absorption at the wavelengths of 532 nm and 355 nm is significant, thus the equations to calculate NLO susceptibilities include the linear absorption coefficient. The model to obtain second-order NLO susceptibility is expressed from equation (6) [72]:

$$\chi^{(2)} = \chi^{(2)}_{Ref}\left(\frac{2}{\pi}\right)\left(\frac{L^{coh}_{Ref}}{d}\right)\sqrt{\frac{I^{2\omega}}{I^{2\omega}_{Ref}}}\left(\frac{\frac{\alpha_{532}d}{2}}{1-\exp\left(-\frac{\alpha_{532}d}{2}\right)}\right) \quad (6)$$

where: $\chi^{(2)}$ is the second-order NLO susceptibility of the studied material, $\chi^{(2)}_{Ref} = 1.0$ pm.V^{-1} [73] denotes the second-order NLO susceptibility of the reference material, d represents the sample thickness, α_{532} signifies the linear absorption coefficient at a wavelength of 532 nm, $I^{2\omega}$ denotes the SHG maximum intensity of the studied material, and $I^{2\omega}_{Ref}$ signifies the maximum intensity of the reference material. $L^{coh}_{Ref} = 21.0$ μm is the coherent length of the reference material, calculated from equation (7):

$$L^{coh}_{Ref} = \frac{\lambda_\omega}{4 \bullet |n_{2\omega} - n_\omega|} \quad (7)$$

where: λ_ω denotes the wavelength of the fundamental beam (1064 nm), while $n_{2\omega}$ is refractive index of reference material at SHG wavelength

Table 7
Selected components of the frequency-dependent α(–ω;ω) and values of ⟨α⟩(–ω;ω) ($\times 10^{-24}$ esu) at ω = 0.04282 a.u. computed by computed by DFT at B3LYP/ 6–31 + G(d), B3LYP/ 3–21 + G, PBE/ 6–31 + G(d), PBE/ 3–21 + G levels of theory for **P1**-**P4**.

Compound	Functional/ Basis set	α_{xx}	α_{yy}	α_{zz}	⟨α⟩
P1	B3LYP/ 6–31 + G(d)	54.639	44.090	51.465	50.065
	B3LYP/ 3–21 + G	52.309	42.254	48.774	47.779
	PBE/ 6–31 + G(d)	34.203	31.292	29.194	31.563
	PBE/ 3–21 + G	34.240	29.808	29.122	31.057
P2	B3LYP/ 6–31 + G(d)	55.428	51.945	50.182	52.518
	B3LYP/ 3–21 + G	53.316	49.844	47.344	50.168
	PBE/ 6–31 + G(d)	38.477	39.051	26.719	34.749
	PBE/ 3–21 + G	36.745	36.730	24.339	32.604
P3	B3LYP/ 6–31 + G(d)	53.234	45.393	59.024	52.550
	B3LYP/ 3–21 + G	51.007	43.067	56.525	50.200
	PBE/ 6–31 + G(d)	32.561	31.174	36.518	33.418
	PBE/ 3–21 + G	33.206	29.240	36.257	32.901
P4	B3LYP/ 6–31 + G(d)	57.025	57.387	63.618	59.343
	B3LYP/ 3–21 + G	54.440	55.005	60.668	56.704
	PBE/ 6–31 + G(d)	35.762	38.962	39.731	38.152
	PBE/ 3–21 + G	34.913	37.600	38.682	37.065

(1.4607) and n_ω is refractive index at fundamental beam (1.4496).

To reveal third-order NLO susceptibility, the relation (8) was used [74,75]:

$$\chi^{(3)} = \chi^{(3)}_{Ref}\left(\frac{2}{\pi}\right)\left(\frac{L^{coh}_{Ref}}{d}\right)\sqrt{\frac{I^{3\omega}}{I^{3\omega}_{Ref}}}\left(\frac{\frac{\alpha_{355}d}{2}}{1-\exp\left(-\frac{\alpha_{355}d}{2}\right)}\right) \quad (8)$$

where: $\chi^{(3)}$ is the third-order NLO susceptibility of the studied material, $\chi^{(3)}_{Ref} = 2.0 \times 10^{-22}$ $m^2.V^{-2}$ [76] denotes the third-order NLO susceptibility of the reference material, α_{355} signifies the linear absorption coefficient at a wavelength of 355 nm, $I^{3\omega}$ denotes the THG maximum intensity of the studied material, and $I^{3\omega}_{Ref}$ signifies the maximum intensity of the reference material, $L^{coh}_{Ref} = 6.7$ μm is the coherent length of the reference material, calculated from equation (9):

$$L^{coh}_{Ref} = \frac{\lambda_\omega}{6 \bullet |n_{3\omega} - n_\omega|} \quad (9)$$

where: λ_ω denotes the wavelength of the fundamental beam (1064 nm), while $n_{3\omega}$ is refractive index of reference material at THG wavelength (1.4761) and n_ω is refractive index at fundamental beam (1.4496).

The NLO susceptibility values found for both polarizations, $\chi^{(2)}$ and $\chi^{(3)}$, are provided in Table 2. The obtained results reveal that changing the substituent from –H (**P1**) to –Br (**P2**) and –OCH_3 (**P3**) enhances the intensity of the SHG signal. Furthermore, the thiazole-azo polymer containing the –Br substituent **P2** demonstrated a higher SHG response compared to the –OCH_3 substituent **P3**, attributed to larger polarizability of –Br compared to methoxy group –OCH_3, which is electron-donating group. Moreover, enhancement was observed compared to the sample containing 2-methyl-5-benzothiazolyl moiety **P4** in comparison to the phenyl ring sample **P3**. This enhancement is explained by the extension of the conjugation length within the polymer. Moreover, we suppose that the large THG values can be explained by increasing electro-donating strength and more efficient charge transfer in **P4**. The strongest THG enhancement was demonstrated by **P4**, which contains 2-methyl-5-benzothiazolyl moiety and –OCH_3 substituent. The obtained values affirm that the values exhibit independence concerning the applied polarization in THG experiment. To provide a better contrast of the obtained second- and third-order NLO susceptibility values, their graphical representations are presented in Fig. 6, marking the value for the reference materials. Notably, **P4** exhibited the strongest NLO response, compared to reference materials widely used in NLO and optoelectronics.

The obtained $\chi^{(2)}$ values were compared with similar styrylquinoline-based polymers reported in the literature [77]. The $\chi^{(2)}$ values for polymers **P1**-**P4**, particularly in the *pp* polarization configuration, demonstrate a notable increase in SHG response compared to $\mathbf{P1_{stq}}$ (0.21 $pm.V^{-1}$ for *sp*; 0.45 $pm.V^{-1}$ for *pp*) [77], a polymer without an electron-acceptor substituent. In contrast to $\mathbf{P1_{stq}}$ [77], which lacks significant SHG response due to the absence of strong electron-donating or electron-withdrawing groups, the polymers **P2** and **P3** from this study incorporate substituents such as –Br and –OCH_3 that simply enhance SHG due to their respective polarizability and electron-donating properties. For $\mathbf{P2_{stq}}$ (0.58 $pm.V^{-1}$ for *sp*; 1.25 $pm.V^{-1}$ for *pp*) [77], where a strong electron-acceptor (NO_2) group is present, a larger NLO response was noted in literature reports, attributed to improved electron

Table 8
Selected components of the frequency-dependent β(–2ω;ω,ω) and β_{tot} ($\times 10^{-30}$ esu) values at ω = 0.04282 a.u. computed by DFT at B3LYP/ 6–31 + G(d), B3LYP/ 3–21 + G, PBE/ 6–31 + G(d), PBE/ 3–21 + G levels of theory for **P1**-**P4.**

Compound	Functional/ Basis set	β_{xxx}	β_{yyy}	β_{zzz}	β_x	β_y	β_z	β_{tot}
P1	B3LYP/ 6–31 + G(d)	−0.555	−0.087	−1.059	−2.568	2.652	−3.510	5.094
	B3LYP/ 3–21 + G	−0.398	−0.411	−0.802	−2.532	1.687	−0.962	3.191
	PBE/ 6–31 + G(d)	−0.035	0.094	−0.860	−2.618	1.892	0.185	3.235
	PBE/ 3–21 + G	0.014	0.188	−0.658	−2.058	2.922	1.228	3.779
P2	B3LYP/ 6–31 + G(d)	−0.256	−2.644	−3.046	−2.498	−5.212	−8.194	10.027
	B3LYP/ 3–21 + G	−0.300	−2.878	−2.343	−2.331	−6.078	−5.363	8.434
	PBE/ 6–31 + G(d)	−0.844	1.398	−0.772	−4.099	6.376	−4.124	8.629
	PBE/ 3–21 + G	−0.518	−1.269	−0.896	−1.786	−2.418	−0.328	3.024
P3	B3LYP/ 6–31 + G(d)	−0.613	−2.222	−1.671	−14.815	−12.582	−9.056	21.443
	B3LYP/ 3–21 + G	−0.294	−2.762	−1.353	−13.011	−13.898	−6.964	20.272
	PBE/ 6–31 + G(d)	0.187	−3.126	0.255	−6.295	−9.958	−1.032	11.826
	PBE/ 3–21 + G	0.158	−2.476	−0.031	−6.104	−8.218	−1.230	10.311
P4	B3LYP/ 6–31 + G(d)	−1.134	0.908	−2.094	−13.203	0.580	−15.444	20.327
	B3LYP/ 3–21 + G	−0.741	0.061	−1.929	−12.381	−1.967	−13.370	18.328
	PBE/ 6–31 + G(d)	0.307	−1.945	−1.436	−7.860	−2.577	−7.860	11.411
	PBE/ 3–21 + G	0.441	−1.377	−1.417	−6.303	−0.971	−7.906	10.158
Urea								0.45 [83]

Table 9
Selected components of the frequency-dependent γ(–3ω;ω,ω,ω) and ⟨γ⟩(–3ω;ω,ω,ω) ($\times 10^{-37}$ esu) values at ω = 0.04282 a.u. computed by DFT at B3LYP/ 6–31 + G(d), B3LYP/ 3–21 + G, PBE/ 6–31 + G(d), PBE/ 3–21 + G levels of theory for **P1**-**P4**.

Compound	Functional/ Basis set	γ_{xxxx}	γ_{yyyy}	γ_{zzzz}	γ_{xxyy}	γ_{xxzz}	γ_{yyzz}	⟨γ⟩
P1	B3LYP/ 6–31 + G(d)	465.269	160.511	168.893	86.376	117.687	116.364	287.105
	B3LYP/ 3–21 + G	407.482	155.394	151.068	77.793	109.384	102.791	258.776
	PBE/ 6–31 + G(d)	160.594	149.490	117.233	23.516	52.072	21.788	124.410
	PBE/ 3–21 + G	185.483	114.968	90.458	30.323	46.276	30.536	121.036
P2	B3LYP/ 6–31 + G(d)	418.420	465.912	250.991	39.157	107.505	113.480	331.121
	B3LYP/ 3–21 + G	376.396	462.260	22.084	32.335	99.693	101.658	265.662
	PBE/ 6–31 + G(d)	237.902	291.904	114.203	5.002	32.435	88.115	179.023
	PBE/ 3–21 + G	239.083	278.720	109.966	1.149	35.444	18.404	147.553
P3	B3LYP/ 6–31 + G(d)	347.816	341.533	277.724	113.736	170.023	190.117	382.965
	B3LYP/ 3–21 + G	300.500	333.336	251.535	98.897	152.005	179.103	349.076
	PBE/ 6–31 + G(d)	81.075	242.510	186.524	13.211	87.591	71.966	171.129
	PBE/ 3–21 + G	122.365	187.946	142.196	20.150	83.164	84.301	165.547
P4	B3LYP/ 6–31 + G(d)	358.757	420.989	308.558	159.475	190.643	235.196	451.786
	B3LYP/ 3–21 + G	313.721	390.639	281.213	151.163	173.824	217.741	414.206
	PBE/ 6–31 + G(d)	64.807	243.440	263.843	58.979	74.104	87.423	202.620
	PBE/ 3–21 + G	84.451	209.922	205.326	58.847	74.987	93.198	190.753
***p*-NA**								127.1 [84]

delocalization. However, among **P2** and **P3**, polymer **P4** from this study shows the highest value (1.03 pm.V^{-1}), likely due to the optimized dipole alignment and backbone structure achieved by incorporating a 2-methyl-5-benzothiazolyl moiety, which facilitates charge transfer. These results suggest that while substituents in **P2** and **P3** polymers moderately enhance the SHG response, further improvements, as seen with **P4**, can be achieved with structures that more effectively enable charge transfer. This information enables the design of polymers with optimized charge transfer, significantly enhancing the efficiency of SHG.

4.5. Computational results and discussion

Quantum chemical calculations have been notified to be available in the depiction of affairs between the electronic structure of items and their optical nonlinearity receptions [78–81]. The theoretical venture allows the assignment of molecular NLO behaviour in a ready technique to plan the structures by testing their talents before syntheses and to appoint hyperpolarizability tensorial portions. The tensor values for hyperpolarizabilities of materials could be declared making use of an adequate theoretical approach. The hyperpolarizability tensors clarify the answer of compounds to an outer electric field. The NLO characters at molecular equalities are established from their static and dynamic hyperpolarizability tensors of components. After conveniently ascertained the geometry optimizations of **P1**-**P4** shown in Fig. 1, the tensorial constituents for β and γ values were calculated from FF technique. Because the static and dynamic quadratic and cubic hyperpolarizabilities relate to the operated functional of DFT, the dispersion-free and frequency-dependent β and γ components were obtained at the DFT criterion utilizing B3LYP functional. In general, the larger dipole moments have direct relevancies with greater projections of β_{tot} amounts [82]. The electric dipole moments, notable components for dispersion-free dipole polarizabilities, quadratic and cubic hyperpolarizabilities computed on **P1**-**P4** are exposed in Tables 3-6, respectively. In this study, the dipole polarizability, second- and third-order hyperpolarizability values were calculated by means of the first (α values), second (β values) and third (γ values) quantitative derivatives of the electric dipole moments according to the enforced field strength in FF approximation. It can be noticed from Table 3 that the calculated μ values for the title polymers acted in the following order **P4** ≅ **P3** > **P1** > **P2** (with B3LYP/ 6–31 + G(d)), **P4** ≅ **P3** > **P1** > **P2** (with B3LYP/ 3–21 + G), **P4** > **P3** > **P1** ≅ **P2** (with PBE/ 6–31 + G(d)), **P4** > **P3** ≅ **P1** > **P2** (with PBE/ 3–21 + G). It is seen that the highest μ values have been obtained at B3LYP/ 6–31 + G(d) level for **P1**-**P4**. To utilize the combination of B3LYP functional and 6–31 + G(d) basis set among the examined materials produced the greatest μ value for **P4** (see Table 3). The computed data for static ⟨α⟩ values in Table 4 have been found in the following order **P4** > **P3** ≅ **P2** > **P1** (with B3LYP/ 6–31 + G(d)), **P4** > **P3** ≅ **P2** > **P1** (with B3LYP/ 3–21 + G), **P4** > **P2** > **P3** > **P1** (with PBE/ 6–31 + G(d)), **P4** > **P3** ≅ **P2** > **P1** (with PBE/ 3–21 + G). The greatest ⟨α⟩ values have been acquired at B3LYP/ 6–31 + G(d) level for **P1**-**P4**. The combination of B3LYP functional and 6–31 + G(d) basis set among **P1**-**P4** gave the highest value of ⟨α⟩ for **P4** (see Table 4). The outputs of static β_{tot} values in Table 5 have been ascertained in the order of **P4** > **P3** > **P2** > **P1** (with B3LYP/ 6–31 + G(d)), **P4** > **P3** > **P2** > **P1** (with B3LYP/ 3–21 + G), **P4** > **P3** > **P2** > **P1** (with PBE/ 6–31 + G(d)), **P4** > **P3** > **P1** > **P2** (with PBE/ 3–21 + G). The highest β_{tot} results have been gotten at B3LYP/ 6–31 + G(d) level for **P1**, **P3**, **P4** and at PBE/ 6–31 + G(d) level for **P2**. The combination of B3LYP functional and 6–31 + G(d) basis set among **P1**-**P4** yielded the greatest conclusion of β_{tot} for **P4** (see Table 5). The static ⟨γ⟩ results in Table 6 have been devised in the order of **P4** > **P3** > **P2** > **P1** (with B3LYP/ 6–31 + G(d)), **P4** > **P3** > **P2** > **P1** (with B3LYP/ 3–21 + G), **P4** > **P2** > **P3** > **P1** (with PBE/ 6–31 + G(d)), **P4** > **P3** > **P2** > **P1** (with PBE/ 3–21 + G). The greatest outputs of ⟨γ⟩ have been arisen at B3LYP/ 6–31 + G(d) level for **P1**, **P3**, **P4** and at B3LYP/ 3–21 + G level for **P2**. The combination of B3LYP functional and 6–31 + G(d) basis set among **P1**-**P4** generated the highest data of ⟨γ⟩ for **P4** (see Table 6).

Tables 7-9, respectively, define a few substantial calculated constituents for dynamic dipole polarizabilities, first and second hyperpolarizabilities of **P1**-**P4**. The calculated data for dynamic ⟨α⟩ values in Table 7 have been obtained in the following order **P4** > **P3** ≅ **P2** > **P1** (with B3LYP/ 6–31 + G(d)), **P4** > **P3** ≅ **P2** > **P1** (with B3LYP/ 3–21 + G), **P4** > **P2** > **P3** > **P1** (with PBE/ 6–31 + G(d)), **P4** > **P3** ≅ **P2** > **P1** (with PBE/ 3–21 + G). The highest frequency-dependent ⟨α⟩ values have been obtained at B3LYP/ 6–31 + G(d) level for **P1**-**P4**. The combination of B3LYP functional and 6–31 + G(d) basis set among **P1**-**P4** produced the highest value of dynamic ⟨α⟩ for **P4** (see Table 7). The results for dynamic β_{tot} values in Table 8 have been found in the order of **P4** ≅ **P3** > **P2** > **P1** (with B3LYP/ 6–31 + G(d)), **P3** > **P4** > **P2** > **P1** (with B3LYP/ 3–21 + G), **P4** ≅ **P3** > **P2** > **P1** (with PBE/ 6–31 + G(d)), **P4** ≅ **P3** > **P1** ≅ **P2** (with PBE/ 3–21 + G). The greatest dynamic β_{tot} conclusions have been yielded at B3LYP/ 6–31 + G(d) level for **P1**-**P4**. The combination of B3LYP functional and 6–31 + G(d) basis set among **P1**-**P4** gave the highest outcomes of β_{tot} for **P4** ≅ **P3** (see Table 8). The

Table 10
The OPA wavelengths (λ_{max}, nm) of the lowest transition, oscillator strengths (*f*) and compositions in terms of MO contributions calculated from TD-SCF/ HF method with cc-pVDZ basis set for **P1**-**P4**.

Compound	State	λ_{max}	f	Composition[a]
P1	S1	416.73	0.0357	H–7 → L
				H–7 → L + 7
				H–6 → L
				H–5 → L
				H–5 → L + 7
				H–2 → L
				H–1 → L
				H → L
				H → L + 7
P2	S1	416.83	0.0365	H–13 → L
				H–8 → L
				H–8 → L + 7
				H–6 → L
				H–5 → L
				H–5 → L + 7
				H–1 → L
				H → L
				H → L + 7
P3	S1	423.45	0.0481	H–12 → L
				H–7 → L
				H–7 → L + 7
				H–6 → L
				H–5 → L
				H–5 → L + 7
				H–1 → L
				H → L
	S2	352.28	0.0399	H–12 → L
				H–7 → L
				H–6 → L
				H–5 → L
				H → L
				H → L + 1
P4	S1	420.58	0.0429	H–14 → L
				H–8 → L
				H–7 → L
				H–6 → L
				H–5 → L
				H–4 → L
				H–1 → L
				H → L
	S2	360.26	0.0213	H–14 → L
				H–8 → L
				H–7 → L
				H–6 → L
				H–5 → L
				H → L
				H → L + 2

[a] H=HOMO, L = LUMO.

Table 11
The calculated first (HOMO, LUMO) and second ((HOMO–1), (LUMO + 1)) frontier MO energies and energy gaps E_g in eV unit using DFT at B3LYP/ 6–31 + G(d) level of theory for **P1**-**P4**.

	P1	P2	P3	P4
HOMO	−5.66	−5.77	−5.42	−5.38
LUMO	−2.60	−2.73	−2.54	−2.55
E_g **[HOMO–LUMO]**	3.06	3.04	2.88	2.83
HOMO–1	−6.73	−6.77	−6.38	−6.35
LUMO + 1	−1.29	−1.45	−1.17	−1.31
E_g **[(HOMO–1)–(LUMO + 1)]**	5.44	5.32	5.21	5.04

dynamic ⟨γ⟩ results in Table 9 have been computed in the order of **P4** > **P3** > **P2** > **P1** (with B3LYP/ 6–31 + G(d)), **P4** > **P3** > **P2** > **P1** (with B3LYP/ 3–21 + G), **P4** > **P2** > **P3** > **P1** (with PBE/ 6–31 + G(d)), **P4** > **P3** > **P2** > **P1** (with PBE/ 3–21 + G). The highest outcomes of dynamic ⟨γ⟩ have been produced at B3LYP/ 6–31 + G(d) level for **P1**-**P4**. The combination of B3LYP functional and 6–31 + G(d) basis set among the investigated compounds here created the greatest conclusion of dynamic ⟨γ⟩ for **P4** (see Table 9).

Our computed data on dynamic quadratic hyperpolarizabilities could be equated with the outcome of urea that is famed as a capacity standard to uncover the second-order NLO quality. The dynamic β_{tot} values computed at B3LYP/ 6–31 + G(d) level with the highest data for **P3** and **P4** have been found 47 and 45, respectively, times higher, that is the greatest factors among the examined structures here, than the first hyperpolarizability of urea ($\beta_{urea} = 0.45 \times 10^{-30}$ esu) affirmed by Ledoux *et al.* [83], but the other examined polymers calculated at B3LYP/ 6–31 + G(d) level have been obtained 22 for **P2** and 11 for **P1** times higher than that of urea (see Table 8). The largest dynamic ⟨γ⟩ value was perceived for **P4** with –OCH_3 electron-donating group and 2-methyl-5-benzothiazolyl moiety that taken away better interaction in the enquired structures and consequently advanced charge transfer guiding to great third-order optical nonlinearity efficiencies. The frequency-dependent ⟨γ⟩ values calculated at B3LYP/ 6–31 + G(d) level with the highest data for title polymers are about factors of 3.5 for **P4**, 3 for **P3**, 2.6 for **P2** and 2.2 for **P1** greater than the cubic hyperpolarizability of *para*-nitroaniline (*p*-NA) ($\gamma_{p\text{-NA}} = 1.271 \times 10^{-35}$ esu) expressed in Ref. [84] that is one of the resource substances used in third-order NLO area (see Table 9).

In this work, the orientationally averaged (isotropic) values of second- and third-order susceptibilities for **P1**-**P4** have been theoretically computed (see Table 2). The calculated consequences for $\langle\chi^{(2)}\rangle$ and $\langle\chi^{(3)}\rangle$ utilizing 6–31 + G(d) and 3–21 + G basis sets are well-coherent with their corresponding experimental outcomes, presenting a propagation in sort order **P4** > **P2** > **P3** > **P1**. The best fit with the measured data ($\chi^{(2)}$, $\chi^{(3)}$) has been calculated using the 6–31 + G(d) diffused and polarized basis set. Both the measured $\chi^{(2)}$, $\chi^{(3)}$ and also computed $\langle\chi^{(2)}\rangle$, $\langle\chi^{(3)}\rangle$ with 6–31 + G(d) and 3–21 + G basis sets exhibit that the quadratic and cubic susceptibilities have the largest and lowest values in the case of **P4** (largest) with –OCH_3 electron-donating group and 2-methyl-5-benzothiazolyl moiety and **P1** (lowest) with –H, respectively. The lowest (for **P1**) and largest (for **P4**) second- and third-order susceptibility conclusions (experimentally $\chi^{(2)}$, $\chi^{(3)}$ and theoretically $\langle\chi^{(2)}\rangle$, $\langle\chi^{(3)}\rangle$) have been analysed on the same structures with their corresponding microscopic data (static and dynamic β_{tot} and ⟨γ⟩), revealing lowest static and dynamic β_{tot} and ⟨γ⟩ for **P1** at PBE/ 6–31 + G(d) level (static β_{tot}), B3LYP/ 3–21 + G level (dynamic β_{tot}), PBE/ 3–21 + G level (static and dynamic ⟨γ⟩) and also, largest static and dynamic β_{tot} and ⟨γ⟩ for **P4** at B3LYP/ 6–31 + G(d) level (static β_{tot} and ⟨γ⟩) and for **P3** ≅ **P4** at B3LYP/ 6–31 + G(d) level (dynamic β_{tot}) and for **P4** at B3LYP/ 6–31 + G(d) level (dynamic ⟨γ⟩) (see Tables 2,5,6,8,9). Altering the substituents in the studied structures here from –H for **P1** to –OCH_3 electron-donating group and 2-methyl-5-benzothiazolyl moiety for **P4** has effectuated the increments on the quadratic and cubic susceptibilities and hyperpolarizabilities (Tables 2,5,6,8,9).

We have computed the vertical pass energies from the ground level to each excited level for **P1**-**P4**, providing the OPA spectra. Fig. 3(b) also exposes the calculated wavelengths (λ_{max}) from TD-SCF/ HF method with cc-pVDZ basis set for the largest values of optical absorptions. The computationally ascertained λ_{max} results of title polymers have understandably well fitted with their corresponding data obtained from measurements, showing transitions in the domains of UV for **P3** and **P4** and Visible for **P1**-**P4** (see Fig. 3(a) and (b)). Table 10 lists the computed maximum absorption wavelengths, oscillator strengths and major contributions belonging to the electronic transmissions of **P1**-**P4**. The title compounds possess compact simulated significant absorption peaks nestled at λ_{max} = 416.73 nm for **P1**, λ_{max} = 416.83 nm for **P2**, λ_{max} = 423.45 and 352.28 nm for **P3**, λ_{max} = 420.58 and 360.26 nm for **P4** with non-zero and relatively great oscillator strengths (Fig. 3(b) and Table 10). Further, to receive some anticipation of the MO attributes, the HOMO and LUMO energies for **P1**-**P4** have been surveyed. The theoretically gained consequences of title compounds on first and second frontier MO energies and their energy gaps are tabulated in Table 11.

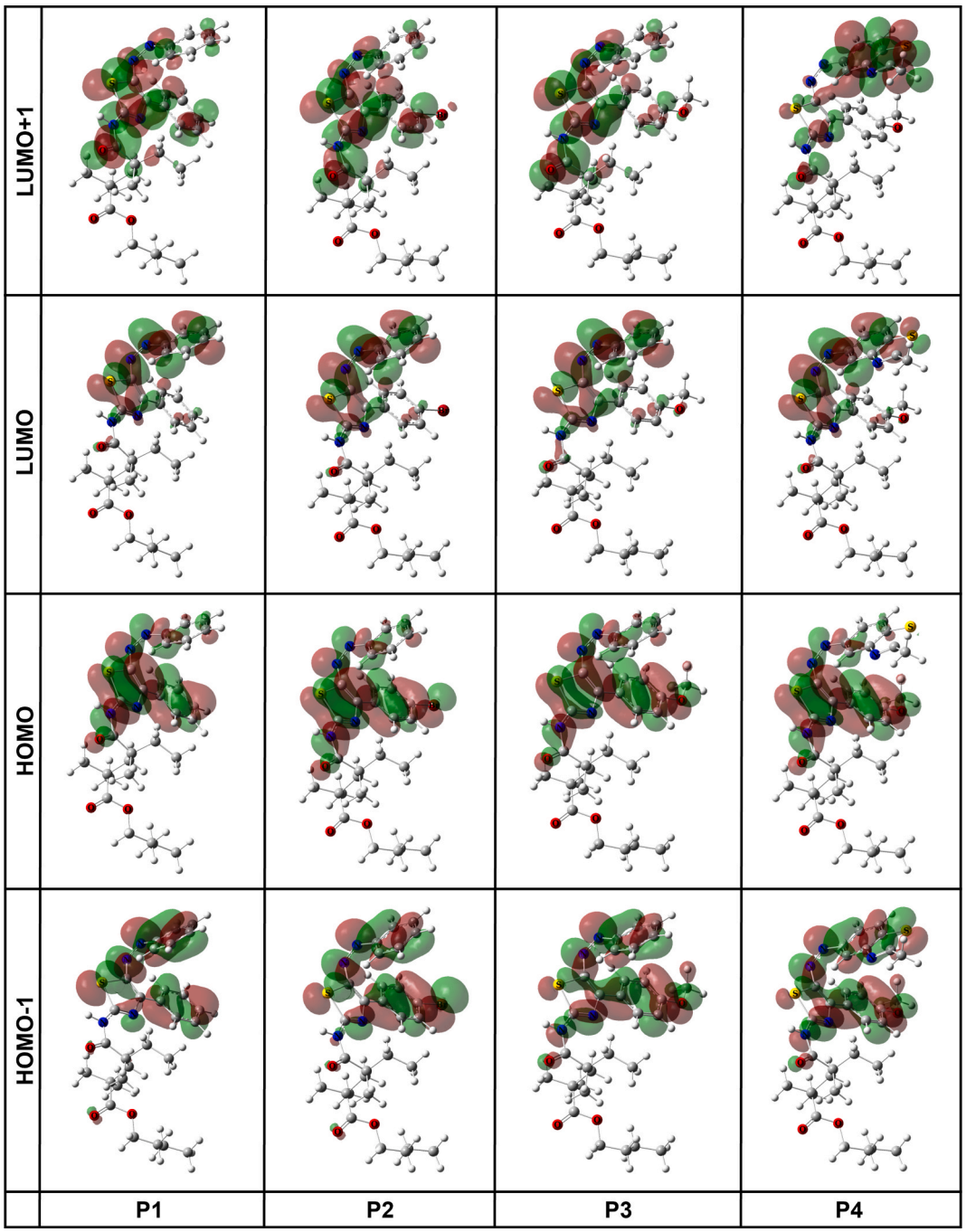

Fig. 7. Selected frontier molecular orbitals of **P1**-**P4** calculated by DFT at B3LYP/ 6–31 + G(d) level of theory.

The plots for all created MOs are submitted in Fig. 7. As realized, when a matter is illuminated through a wavelength of light (λ) with energy equal to HOMO-LUMO energy gap (E_g), λ is radiated or absorbed and the energy is operated to transmit any electron from the HOMO to the LUMO. The HOMO-LUMO energy gap for a thiazole-based polymer donor (namely PSZ) was reported by DFT/ B3LYP as 2.0 eV in Ref. [85]. Osman [86] calculated the HOMO-LUMO energy gaps as E_g = 2.426, 2.440, 2.235 eV for A, B, C three thiazole azo dyes, respectively, from DFT/ B3LYP. Our calculated conclusions on HOMO-LUMO energy gaps of **P1**-**P4** (E_g = 3.06 (**P1**), 3.04 (**P2**), 2.88 (**P3**), 2.83 eV (**P4**)) is understandably adjacent to the appraised data for similar thiazole-azo materials by Ref. [85,86] (see Table 11).

Since the quadratic and cubic NLO responses are affected by charge transfer stimulations covering HOMO and LUMO, the higher second- and third-order hyperpolarizability components and susceptibilities can be maintained by lower HOMO-LUMO energy gaps [87]. In this way, it might be supposed that all investigated materials with pretty low HOMO-LUMO energy gaps with the lowest value for **P4**, could have quadratic and cubic NLO properties with non-zero and rather great reactions with the highest values for **P4** (see Tables 2,5,6,8,9,11). The HOMOs and HOMO–1 s of **P1**-**P4** are almost identical and expressly seated on both aromatic 4-aryl-1,3-thiazol-2-amine rings and also electron-donating for **P1**, **P3** and **P4** and electron-withdrawing groups for **P2** linked to aromatic moieties, while the LUMOs and LUMO + 1 s are especially nestled on aromatic 4-aryl-1,3-thiazol-2-amine rings and partly on electron-donating for **P1**, **P3** and **P4** and electron-withdrawing groups for **P2** linked to aromatic moieties (see Fig. 7).

5. Conclusions

This study investigated the impact of various chemical substituents on the NLO performance of thiazole-azo polymer thin films, specifically their SHG and THG properties. The results show that these polymers exhibit significant NLO responses, with the highest efficiency observed for **P4**, which benefited from optimized charge transfer facilitated by the 2-methyl-5-benzothiazolyl moiety. SHG studies demonstrated similar intensity across polymers **P1**-**P4**, highlighting the importance of the polymer backbone's intrinsic symmetry and electronic structure. Comparing our findings with previous styrylquinoline-based polymers, thiazole-azo polymers exhibited higher SHG values than counterparts like $\mathbf{P1}_{\mathbf{stq}}$ [77]. The influence of substituents was also evident, with **P4** outperforming the others in both SHG and THG responses. The molecular design, particularly the electron-donating and electron-withdrawing substituents, played a key role in optimizing the charge transfer properties, further enhancing NLO efficiency. Theoretical calculations provided insights into the second- and third-order susceptibilities, which were well aligned with experimental data. The best agreement between the experimental and theoretical results for the optical nonlinearity behaviour of the studied materials was obtained using the 6–31 + G(d) diffused and polarized basis set, combined with the B3LYP functional operated in our computations. While discrepancies between experimental and theoretical values may arise from computational approximations, it should be noted that some numerical differences may also result from inefficiencies in basis set and functional choices. Our basis set and functional preferences in computational studies may not fully match the molecular states of **P1**-**P4** observed experimentally. Nonetheless, the chosen methodology offers a successful description of the molecular states and NLO properties. Besides, sources of experimental errors, such as laser power fluctuations, may also contribute to differences between the measured and calculated values. These findings suggest that thiazole-azo polymers, with tailored molecular designs, are promising candidates for advanced optoelectronic and NLO applications.

Declaration of competing interest

The authors declare that they have no known competing financial interests or personal relationships that could have appeared to influence the work reported in this paper.

Acknowledgements

This work was supported partly by Ministry of Education and Science of Ukraine within the projects "Polymer systems and nanocomposites for optoelectronics" (no. 0124U001177) and Partly by the project TeraHertz that has received funding from the H2020 EU project: TeraHertz (2023_00057) Staff exchanges projects: Marie Skłodowska-Curie Actions Developing talents, advancing research (2023-2028) grant agreement nr 101086493 entitled as "Novel Technologies and Materials for TeraHertz Radiation Control".

Appendix A. Supplementary data

Supplementary data to this article can be found online at https://doi.org/10.1016/j.saa.2025.126495.

Data availability

Data will be made available on request.

References

[1] Y. Zeng, C.-L. Hu, W.-J. Xu, T.-W. Zeng, Z.-X. Zhu, X.-X. Chen, D.-X. Liu, Y.-J. Chen, Y.-B. Zhang, W.-X. Zhang, X.-M. Chen, *Angew. Chem.* 61 (2) (2022) e202110082.
[2] M. Kalmutzki, M. Ströbele, F. Wackenhut, A.J. Meixner, H.-J. Meyer, *Angew. Chem.* 55 (2014) 14260–14263.
[3] P. Hanczyc, M. Samoc, B. Norden, *Nat. Photon.* 7 (2013) 969–972.
[4] E. Garmire, *Opt. Express* 21 (25) (2013) 30532–30544.
[5] N. Chauvet, M.E. de Corny, M. Jeannin, G. Laurent, S. Huant, T. Gacoin, G. Dantelle, G. Nogues, G. Bachelier, *ACS Photonics* 7 (3) (2020) 665–672.
[6] L. Meng, A. Padhye, C. Pedersen, M. Ebrahim-Zadeh, P.J. Rodrigo, *Opt. Lett.* 44 (7) (2019) 1670–1673.
[7] A. Nair, C.-Y. Lin, F.-C. Hsu, T.-H. Wong, S.-C. Chuang, Y.-S. Lin, C.-H. Chen, P. Campagnola, C.-H. Lien, S.-J. Chen, *Sci. Rep.* 13 (2023) 19534.
[8] I. Miler, M.D. Rabasovic, M. Aleksic, A.J. Krmpot, A. Kalezic, A. Jankovic, B. Korac, A. Korac, *J. Biophotonics* 14 (3) (2021) e202000362.
[9] Y. Ling, C. Li, K. Feng, S. Palmer, P.L. Appleton, S. Lang, D. McGloin, Z. Huang, G. Nabi, *J. Biophotonics* 10 (6–7) (2017) 911–918.
[10] J. Chen, C.-L. Hu, F. Kong, J.-G. Mao, *Acc. Chem. Res.* 54 (12) (2021) 2775–2783.
[11] B. Zerulla, A. Luna Díaz, C. Holzer, C. Rockstuhl, I. Fernandez-Corbaton, M. Krstić, *Adv. Opt. Mater.* 12 (18) (2024) 2400150.
[12] D. Hähnel, C. Golla, M. Albert, T. Zentgraf, V. Myroshnychenko, J. Förstner, C. Meier, *Light Sci. Appl.* 12 (2023) 97.
[13] S. Hong, Y. Xie, M. Tan, Y. Li, M. Ding, L. Zhang, Z. Yu, K. Wang, A.D. Ellis, D. Dai, *ACS Photonics* 12 (2) (2025) 1146–1154.
[14] X. Ma, W. Chen, L. Tong, S. Liu, W. Dai, S. Ye, Z. Zheng, Y. Wang, Y. Zhou, W. Zhang, W. Fang, X. Chen, M. Liao, W. Gao, *Opt. Laser Technol.* 143 (2021) 107286.
[15] A. Mushtaq, B. Pradhan, D. Kushavah, Y. Zhang, M. Wolf, N. Schrenker, E. Fron, S. Bals, J. Hofkens, E. Debroye, S.K. Pal, *ACS Photonics* 8 (11) (2021) 3365–3374.
[16] S. Abdallah, R. Mhanna, J. Cabrera-González, R. Núñez, A. Khitous, F. Morlet-Savary, O. Soppera, D.-L. Versace, J.-P. Malval, *Chem. Mater.* 35 (17) (2023) 6979–6989.
[17] B.J. Furey, B.J. Stacy, T. Shah, R.M. Barba-Barba, R. Carriles, A. Bernal, B. S. Mendoza, B.A. Korgel, M.C. Downer, *ACS Nano* 16 (4) (2022) 6023–6033.
[18] Q. Liu, S. Hu, C. Zhang, H. Ouyang, T. Jiang, *Adv. Opt. Mater.* 9 (1) (2021) 2001562.
[19] P. Sun, Y. Sun, H. Yang, X. Xu, Y. Jin, S. He, *Laser Photonics Rev.* 18 (4) (2024) 2300263.
[20] X. Li, Y. Tan, L. Yin, Y. Huo, L. Zhao, Q. Yue, T. Ning, *Opt. Lett.* 46 (5) (2021) 1029–1032.
[21] A.S.S. Reddy, A.V. Kityk, J. Jedryka, N. Purnachand, P. Rakus, A. Wojciechowski, A.S. Andrushchak, V.R. Kumar, N. Veeraiah, *Opt. Mater.* 123 (2022) 111858.
[22] Y. Farah, G. Murray, J. Field, M. Varughese, L. Wang, O. Pinaud, R. Bartels, *Optica* 11 (5) (2024) 693–705.
[23] L.-T. Chou, H.-H. Hung, A.-Y. Liu, S.-H. Wu, J.-C. Jang, D.-L. Zhong, H.-H. Hsiao, S.-H. Chia, *Laser Photonics Rev.* 17 (7) (2023) 2200297.
[24] K. Geng, X. Yang, Y. Zhao, Y. Cui, J. Ding, H. Hou, *Inorg. Chem.* 61 (2022) 12386–12395.
[25] C.W. Ghanavatkar, V.R. Mishra, N. Sekar, *Dyes Pigm.* 191 (2021) 109367.
[26] F. Cuétara-Guadarrama, M. Vonlanthen, K. Sorroza-Martínez, I. González-Méndez, E. Rivera, *Dyes Pigm.* 194 (2021) 109551.
[27] C. Naim, F. Castet, E. Matito, *Phys. Chem. Chem. Phys.* 23 (2021) 21227–21239.
[28] H. Wang, F. Chen, *J. Phys. Chem. A* 127 (23) (2023) 5030–5038.
[29] A. De Girolamo Del, F. Mauro, F. Loffredo, M.F. Villani, T. Caso, A. Fasolino, D. Vestri, A. Sagnelli, L. D'Avino, G.N. Petti, *Proc. SPIE* 12584 (2023) 125840B.
[30] M. Dudek, A. Kaczmarek-Kędziera, R. Deska, J. Trojnar, P. Jasik, P. Młynarz, M. Samoć, K. Matczyszyn, *J. Phys. Chem. B* 126 (32) (2022) 6063–6073.
[31] D. Chomicki, O. Kharchenko, L. Skowronski, J. Kowalonek, A. Kozanecka-Szmigiel, D. Szmigiel, V. Smokal, O. Krupka, B. Derkowska-Zielinska, *Int. J. Mol. Sci.* 21 (2020) 5755.
[32] B. Derkowska-Zielinska, O. Krupka, V. Smokal, A. Grabowski, M. Naparty, L. Skowronski, *Mol. Cryst. Liq. Cryst.* 639 (2016) 87–93.
[33] X. Yu, Z. Wang, M. Buchholz, N. Füllgrabe, S. Grosjean, F. Bebensee, S. Bräse, C. Wöll, L. Heinke, *Phys. Chem. Chem. Phys.* 17 (2015) 22721–22725.
[34] G. Li, M. Xu, S. Zhang, G. Yang, W. Li, *Macromol. Rapid Commun.* 43 (2022) 2100904.
[35] J. Konieczkowska, A. Wasiak, A. Sobolewska, S. Bartkiewicz, J.G. Małecki, E. Schab-Balcerzak, *J. Photochem. Photobiol. A: Chem.* 444 (2023) 114979.
[36] H. Ren, P. Yang, F.M. Winnik, *Polym. Chem.* 11 (2020) 5955.
[37] B. Derkowska-Zielinska, L. Skowronski, T. Kozlowski, V. Smokal, A. Kysil, A. Biitseva, O. Krupka, *Opt. Mater.* 49 (2015) 325–329.
[38] B. Derkowska-Zielinska, L. Skowronski, M. Sypniewska, D. Chomicki, V. Smokal, O. Kharchenko, M. Naparty, O. Krupka, *Opt. Mater.* 85 (2018) 391–398.
[39] S.W. Basuki, V. Schneider, T. Strunskus, M. Elbahri, F. Faupel, A.C.S. Appl, *Mater. Interfaces* 7 (2015) 11257–11262.
[40] Z. Ma, J. Wu, Y. Tan, C. Tan, *Macromol. Rapid Commun.* 45 (12) (2024) 2400048.
[41] S. Chiodini, F. Borbone, S.L. Oscurato, P.D. Garcia, A. Ambrosio, *Nanophotonics* 13 (2) (2024) 229–238.
[42] Y. Huang, Y. Zhu, L. Cao, Y. Jing, Z. Xu, G. Tang, Y. Shu, X. Liu, X. Zhang, *J. Appl. Polym. Sci.* 142 (10) (2025) e56550.
[43] Y. Skrypka, V. Kokars, K. Traskovskis, A. Ozols, P. Augustovs, A. Shumelyuk, S. Odoulov, *Opt. Continuum* 1 (4) (2022) 885–895.
[44] S. Moujdi, Y. Bougdid, A. Rahmouni, T. Mahfoud, D. Nesterenko, M. Halim, Z. Sekkat, *Proc. SPIE* 10944 (2019) 1094403.
[45] S.H. Alotaibi, A.S. Radwan, Y.K. Abdel-Monem, M.M. Makhlouf, *Spectrochim. Acta A Mol. Biomol. Spectrosc.* 205 (2018) 364–375.
[46] H.S. Deshmukh, V.A. Adole, A. Kumar, N. Misra, S.D. Pawar, S.R. Tambe, B. S. Jagdale, *J. Mol. Struct.* 1305 (2024) 137745.
[47] O.I. Osman, *Int. J. Mol. Sci.* 18 (2) (2017) 239.

[48] R.M. El-Shishtawy, F. Borbone, Z.M. Al-amshany, A. Tuzi, A. Barsella, A.M. Asiri, A. Roviello, *Dyes Pigm.* 96 (1) (2013) 45–51.
[49] M.M.M. Raposo, A.M.C. Fonseca, M.C.R. Castro, M. Belsley, M.F.S. Cardoso, L. M. Carvalho, P.J. Coelho, *Dyes Pigm.* 91 (1) (2011) 62–73.
[50] K. Venkatesha, K. Sheela, M.S. Srinivas, A. Swamynayaka, M. Madegowda, T. A. Hegde, M.P. Sadashiva, *J. Mol. Struct.* 1319 (2) (2025) 139459.
[51] P.D. Maker, R.W. Terhune, M. Nisenoff, C.M. Savage, *Phys. Rev. Lett.* 8 (1962) 21.
[52] A. Szukalski, B. Sahraoui, B. Kulyk, C.A. Lazar, A.M. Manea, J. Mysliwiec, *RSC Adv.* 7 (2017) 9941–9947.
[53] A. Szukalski, K. Parafiniuk, K. Haupa, W. Goldeman, B. Sahraoui, F. Kajzar, J. Mysliwiec, *Dyes Pigm.* 142 (2017) 507–515.
[54] R.A. Myers, N. Mukherjee, S.R.J. Brueck, *Opt. Lett.* 16 (1991) 1732–1734.
[55] B. Sahraoui, J. Luc, A. Meghea, R. Czaplicki, J.L. Fillaut, A. Migalska-Zalas, *J. Opt. A: Pure Appl. Opt.* 11 (2009) 024005.
[56] K.A. Kurtz, J.J.P. Stewart, K.M. Dieter, *J. Comput. Chem.* 11 (1990) 82–87.
[57] H.D. Cohen, C.C. Roothaan, *J. Chem. Phys.* 43 (1965) S34–S39.
[58] M. J. Frisch, et al., Gaussian 09, Revision D.01, Gaussian, Inc., Wallingford CT, 2009.
[59] R. Dennington, T. Keith, J. Millam, GaussView, Version 5.0.9; Semichem Inc.: Shawnee Mission, KS, 2009.
[60] G. Te Velde, F.M. Bickelhaupt, E.J. Baerends, C. Fonseca Guerra, S.J.A. van Gisbergen, J.G. Snijders, T. Ziegler, *J. Comput. Chem.* 22 (2001) 931–967.
[61] I.C. De Silva, R.M. de Silva, K.M. Nalin de Silva, *J. Mol. Struct.: THEOCHEM* 728 (2005) 141–145.
[62] C. Mang, K. Wu, *Int. J. Quantum Chem.* 106 (2006) 2529–2535.
[63] P.L. Franzen, S.C. Zilio, A.E.H. Machado, J.M. Madurro, A.G. Brito-Madurro, L. T. Ueno, R.N. Sampaio, N.M. Barbosa Neto, *J. Mol. Struct.* 892 (2008) 254–260.
[64] J.P. Perdew, K. Burke, M. Ernzerhof, *Phys. Rev. Lett.* 77 (1996) 3865.
[65] K.S. Thanthiriwatte, K.M. Nalin de Silva, *J. Mol. Struct.: THEOCHEM* 617 (2002) 169–175.
[66] M.W. Schmidt, K.K. Baldridge, J.A. Boatz, S.T. Elbert, M.S. Gordon, J.H. Jensen, S. Koseki, N. Matsunaga, K.A. Nguyen, S. Su, et al., *J. Comput. Chem.* 14 (1993) 1347–1363.
[67] D. Trefon-Radziejewska, G. Hamaoui, M. Chirtoc, N. Horny, V. Smokal, A. Biitseva, O. Krupka, B. Derkowska-Zielinska, *Mater. Chem. Phys.* 223 (2018) 700–707.
[68] B. Derkowska-Zielinska, L. Skowronski, A. Biitseva, A. Grabowski, M. Naparty, V. Smokal, A. Kysil, O. Krupka, *Appl. Surf. Sci.* 421 (2017) 361–366.
[69] B. Kulyk, D. Guichaoua, A. Ayadi, A. El-Ghayoury, B. Sahraoui, *Dyes Pigm.* 145 (2017) 256–262.
[70] R.W. Boyd, *Nonlinear Optics*, 3rd ed., Academic Press, 2003.
[71] P.N. Prasad, D.J. Williams, *Introduction to Nonlinear Optical Effects in Molecules & Polymers*, Wiley, New York, 1991.
[72] G.J. Lee, S.W. Cha, S.J. Jeon, J.I. Jin, J.S. Yoon, *J. Korean Phys. Soc.* 39 (2001) 912–915.
[73] F. Kajzar, Y. Okada-Shudo, C. Meritt, Z. Kafafi, *Synth. Met.* 117 (2001) 189–193.
[74] K. Kubodera, H. Kobayashi, *Mol. Cryst Liq. Cryst. Incorporating Nonlinear Optics* 182 (1990) 103–113.
[75] H. Kobayashi, H. Kanbara, M. Koga, K. Kubodera, *J. Appl. Phys.* 74 (1993) 3683–3687.
[76] X.H. Wang, D.P. West, N.B. McKeown, T.A. King, *J. Opt. Soc. Am. B* 15 (1998) 1895–1903.
[77] D. Guichaoua, B. Kulyk, V. Smokal, A. Migalska-Zalas, O. Kharchenko, O. Krupka, O. Kolendo, B. Sahraoui, *Org. Electron.* 66 (2019) 175–182.
[78] D.M. Burland, R.D. Miller, C.A. Walsh, *Chem. Rev.* 94 (1994) 31–75.
[79] B.-H. Lei, S. Pan, Z. Yang, C. Cao, D.J. Singh, *Phys. Rev. Lett.* 125 (2020) 187402.
[80] M.U. Khan, S. Hussain, M.A. Asghar, K.S. Munawar, R.A. Khera, M. Imran, M. M. Ibrahim, M.M. Hessien, G.A.M. Mersal, *ACS Omega* 7 (2022) 18027–18040.
[81] R. Bano, M. Asghar, K. Ayub, T. Mahmood, J. Iqbal, S. Tabassum, R. Zakaria, M. A. Gilani, *Front. Mater.* 8 (2021) 783239.
[82] S.M. Risser, D.N. Beratan, S.R. Marder, *J. Am. Chem. Soc.* 115 (1993) 7719–7728.
[83] I. Ledoux, J. Zyss, *Chem. Phys.* 73 (1982) 203–213.
[84] H.S. Nalwa, S. Miyata, *Nonlinear Optics of Organic Molecules and Polymers*, CRC Press, New York, 1997.
[85] Y. Xu, H. Yao, T. Zhang, L. Ma, J. Hou, *Trans. Tianjin Univ.* 28 (2022) 398–405.
[86] O.I. Osman, *Int. J. Mol. Sci.* 18 (2017) 239.
[87] P.S. Liyanage, R.M. de Silva, K.M.N. de Silva, *J. Mol. Struct.: THEOCHEM* 639 (2003) 195–201.